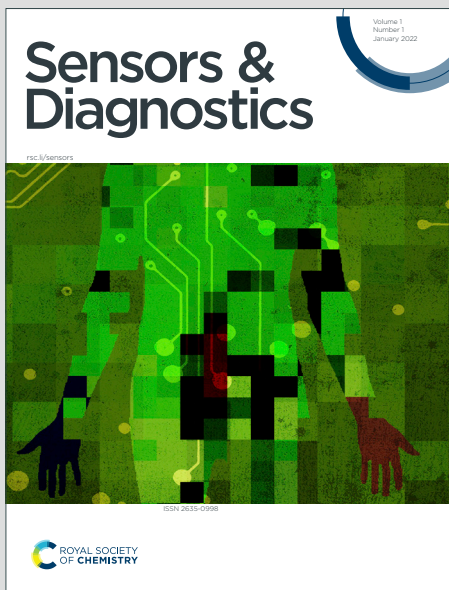


Sensors & Diagnostics

Accepted Manuscript

This article can be cited before page numbers have been issued, to do this please use: N. Ganesan, K. Srinivasan, E. Antony, M. hab. Jan G., A. N. Sukumar, A. Abiram, J. Prabhu and N. Raju, *Sens. Diagn.*, 2025, DOI: 10.1039/D5SD00202H.



This is an Accepted Manuscript, which has been through the Royal Society of Chemistry peer review process and has been accepted for publication.

Accepted Manuscripts are published online shortly after acceptance, before technical editing, formatting and proof reading. Using this free service, authors can make their results available to the community, in citable form, before we publish the edited article. We will replace this Accepted Manuscript with the edited and formatted Advance Article as soon as it is available.

You can find more information about Accepted Manuscripts in the [Information for Authors](#).

Please note that technical editing may introduce minor changes to the text and/or graphics, which may alter content. The journal's standard [Terms & Conditions](#) and the [Ethical guidelines](#) still apply. In no event shall the Royal Society of Chemistry be held responsible for any errors or omissions in this Accepted Manuscript or any consequences arising from the use of any information it contains.

ICT-Driven Ag^+ Detection Using Xylene-spacer integrated Naphthalene Probes as Fluorescent Chemosensors: Selectivity, Practical Monitoring, and Anticounterfeiting

Narmatha Ganesan^a, Kavanya Srinivasan^a, Elizabeth Antony^a, hab. Jan G. Malecki^b, Abisha Nancy Sukumar^c, Abiram Angamuthu^{d,*}, J. Prabhu^a, Raju Nandhakumar^{a,*}

^aFluorescent Materials Lab, Division of Physical Science, Karunya Institute of Technology and Sciences, (Deemed-to-be University), Karunya Nagar, Coimbatore - 641 114, India.

*E-mail: nandhakumar@karunya.edu

^bInstitute of Chemistry, University of Silesia, Szkolna 9 str. 40-006 Katowice.

^cDepartment of physics, Karpagam College of Engineering, Coimbatore, Tamil Nadu, India

^dDepartment of physics, Rathinam Technical Campus, Coimbatore- 641021, Tamil Nadu, India

*E-mail: aabiram@gmail.com

Abstract

Two xylene-linked naphthalene-based fluorescent probes, **ONA** and **MNA**, were designed, synthesized and fully characterized by NMR and mass spectrometry for the selective detection of Ag^+ ions. In a $\text{MeOH}:\text{H}_2\text{O}$ (1:1, v/v) medium at physiological pH (7.3), both probes exhibited pronounced selectivity and high sensitivity toward Ag^+ . The sensing response arises from a synergistic mechanism involving restriction of C–O bond rotation, suppression of the intramolecular charge transfer (ICT) process, and chelation-induced complex stabilization, leading to enhanced fluorescence accompanied by a hypsochromic shift. Quantitative evaluation through quantum yield measurements, limits of detection, and binding constant analysis confirmed efficient Ag^+ recognition. The practical applicability of the probes was validated through successful detection in real samples, including millets, vegetables, ointments, and soils, as well as bacterial imaging in *E. coli* and anticounterfeiting stamping applications. These results establish **ONA** and **MNA** as versatile and multifunctional fluorescent chemosensors for Ag^+ detection.

Keywords: Naphthalene, Silver ions, blue shift, ICT, stamp-ink method, Bio-imaging

1. INTRODUCTION

The positively charged silver ion (Ag^+) acts as a potent broad-spectrum antimicrobial agent by inhibiting the growth of and ultimately destroying, a wide range of microorganisms including bacteria, fungi, and viruses. It exerts its effect primarily by binding to cellular membranes and biomolecules, disrupting membrane integrity, interfering with enzymatic activity, and causing irreversible damage to nucleic acids, which collectively leads to microbial death^{1–3}. Due to these functions, Ag^+ ions have been applied in a wide range of applications like wound care, water purification, antimicrobial coating for medical devices and consumer products^{4,5}. Silver ions (Ag^+) are generally considered to have low toxicity to humans in most practical applications. However, chronic or excessive exposure, particularly via inhalation of colloidal silver, can result in argyria, a condition characterized by irreversible bluish-gray skin discoloration. In addition to their broad-spectrum antimicrobial action, Ag^+ ion technology is also effective in preventing the formation of biofilms, which are structured microbial communities known for their extreme resistance to conventional disinfectants^{6,7}. Silver is one of the most commonly used noble metals in various industries such as photography, electronics, catalysis, and particularly food and medicine^{8–10}. The therapeutic application of Ag^+ involves its application for dressing wounds, creams and as an antibiotic coating^{11–13}. Wound dressings with silver sulfadiazine or silver nanoparticles are used to treat surface infections¹⁴. Nevertheless, significant concerns persist regarding the indiscriminate and excessive release of silver ions (Ag^+) into the environment^{15–17}. It is well documented that high levels of Ag^+ induce cytotoxicity, bioaccumulation and disruption of enzymatic processes and all of which have significant implications to human health as well as aquatic life^{18–21}. Therefore, stringent limits have been established by the World Health Organization (WHO) on silver content in drinking water emphasizing the immense need for analytical methods to determine it accurately²².

Over the past few years, researchers have made significant efforts toward the design of molecular probes that are highly sensitive and selective for the detection of Ag^+ ions. owing to their capacity for rapid, affordable and non-destructive detection. These sensors can convert the binding interaction of Ag^+ into an observable optical signal, often

visible as fluorescence enhancement, quenching or emission shifts. They are therefore very well suited for use in real-world applications, such as water quality monitoring in real time, sensing in food and cosmetic samples, logic gate systems and even biological imaging. A major challenge in developing effective Ag^+ sensors is achieving high selectivity, since Ag^+ shares close chemical similarity with other soft metal ions such as Hg^{2+} , Pb^{2+} , and Cd^{2+} . To overcome this limitation, considerable effort has focused on designing molecular scaffolds bearing sulfur, amine or heteroaromatic donor groups, exploiting the strong affinity of Ag^+ for soft Lewis bases. Additionally, supramolecular approaches, including the integration of Ag^+ binding sites within conjugated fluorophores, have proven effective at maximizing sensitivity and tunability^{23,24}. Such developments demonstrate the utility of fluorescent chemosensors as useful tools for sensing silver contamination in environmental and biological systems.

Conventional analytical techniques for Ag^+ detection, such as voltammetry, inductively coupled plasma mass spectrometry (ICP-MS), and atomic absorption spectroscopy (AAS) are well established and offer extremely high sensitivity and precision^{25,26}. These techniques are not necessarily best for quick or on-site analysis because they demand costly equipment and labor-intensive sample preparation. Fluorescent-based chemosensors have become popular substitutes in this environment because of their high sensitivity, selectivity, fast reaction, ease of use and real-time monitoring ability. Fluorescence chemosensors for Ag^+ typically operate through one or more photophysical processes such as photoinduced electron transfer (PET), intramolecular charge transfer (ICT), excimer/exciplex formation, aggregation-induced emission (AIE), or fluorescence resonance energy transfer (FRET). The interaction of Ag^+ with particular donor atoms (nitrogen, oxygen or sulfur) or π -conjugated systems often causes apparent photophysical changes that can be used for ratiometric, "turn-on," or "turn-off" fluorescence responses²⁷⁻²⁹. The logical architecture of these sensors not only allows for accurate identification of Ag^+ ions in biological and environmental samples but also gives insightful knowledge on its coordinating chemistry. Hence, developing selective and effective fluorescent chemosensors for Ag^+ ions remains a popular area of research with significant consequences for medical applications, food safety, and

environmental monitoring based on the Fluorescence Organic Molecules (FOM's) like rhodamine, benzimidazole, Schiff base and thiourea based chemosensors^{30–33}. The significance of fluorescence chemosensors is particularly notable in the realm of anticounterfeiting. Counterfeit products, including spurious medicines, foodstuffs, cosmetics and currency, inflict substantial economic damage and pose serious health risks. Fortunately, fluorescence chemosensors offer a sophisticated solution to this problem. By generating unique light signals, such as a change in color or emission of light under UV illumination, these chemosensors provide a reliable means of authentication that is difficult to replicate. By incorporating such sensors on packaging, labels, or product coatings, it is possible to swiftly verify authenticity by the naked eye or basic portable equipment. Their ease of visualization, high sensitivity and low price make fluorescent chemosensors an effective measure for the prevention of counterfeiting and consumer safety. Among the methods, the stamping-ink method is one of the best method for preventing the document forgery^{34,35}.

On continuation of our works on fluorescent organic molecules, two novel xylene-based fluorescence chemosensor, namely **ONA** and **MNA**, were designed for the selective detection of Ag^+ ions. In this modular design, the naphthalene scaffolds act as the fluorophores, the oxygen atoms as the ionophores and the xylelene moiety as the spacer. The probe's functionality relies on the binding of carbonyl oxygen (C=O) and ether group (C-O) with Ag^+ ions, resulting in the restriction of C-O rotation and inhibition of the Intramolecular Charge Transfer (ICT) process. This leads to a hypsochromic shift through the formation of chelation-enhanced fluorescence (CHEF). Both **ONA** and **MNA** probes were successfully utilized for detecting Ag^+ ions in real-world sample analysis, visualizing soil samples, and cell imaging using *E. coli* bacteria. Furthermore, the complexation solution was used to develop an invisible fluorescence stamping method.

2. EXPERIMENTAL SECTION

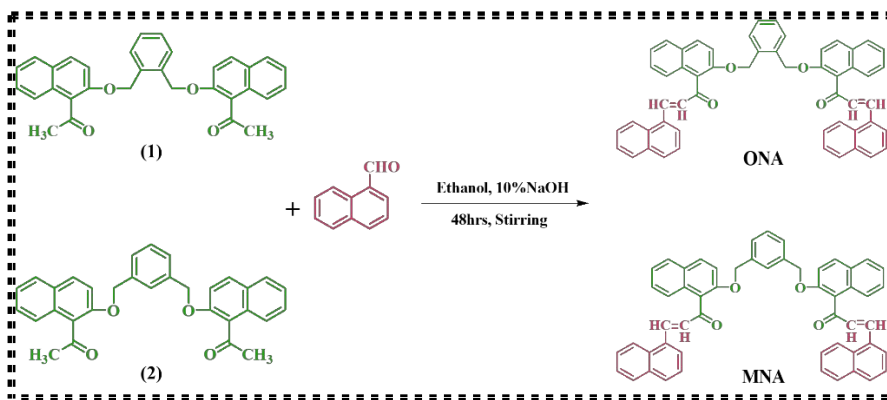
Materials and Instrumentation – supporting information.

Synthesis of probes **ONA** and **MNA**

Synthesis of ONA: The compound **1** was synthesized by the reaction of dibromo ortho-xylene with 2-hydroxy acetonaphthone in the presence of potassium carbonate (K_2CO_3) as a base, utilizing acetonitrile as the solvent³⁶. Synthesis of probe **ONA** is obtained by treating compound **1** (0.20 g, 0.0004 mmol) dissolved in absolute ethanol (10 mL) and stirred under room temperature with 1-naphthaldehyde (0.13 g, 0.0008 mmol) in the presence of 10% NaOH. The reaction was monitored by thin-layer chromatography (TLC) and upon completion, the mixture was neutralized with dilute hydrochloric acid (HCl). Subsequently, a water-chloroform separation was performed to remove excess base. The solvent was then evaporated and the resulting residue was recrystallized using chloroform to yield the target compound, **ONA**, as a solid. Yield : 72%. 1H NMR (300 MHz, $CDCl_3$): 8.21-8.17 (d, 1H), 7.79-7.54 (q, 4H), 7.48-7.47 (d, 1H), 7.45-7.29 (m, 6H), 7.13 (s, 1H) 7.09-7.06 (m, 4H), 5.28 (s, 2H) ppm. ^{13}C NMR (75 MHz, $CDCl_3$): 196.63, 153.41, 142.22, 134.62, 133.59, 131.81, 131.59, 131.27, 130.74, 129.16, 128.99, 128.69, 128.18, 127.58, 126.83, 126.15, 125.41, 125.35, 124.27, 124.21, 123.16, 114.43, 69.52 ppm. LC – MS calcd for $C_{54}H_{38}O_4$: $[M^+]$ 750.89, found $[M^+ + H]^+$ 751.19 (Figure. S1, S3, S5) (Scheme.1). This structure was further confirmed by single crystal XRD analysis with CCDC 2490615 and other data (Figure. S19, Table. S2).

Synthesis of MNA: The compound **2** was synthesized by the mixture of dibromo meta-xylene with 2-hydroxy acetonaphthone in the presence of a base, potassium carbonate by using acetonitrile as solvent³⁶. Synthesis of probe **MNA** is obtained by treating compound **1** (0.20 g, 0.0004 mmol) dissolved in absolute ethanol (10 mL) and stirred under room temperature with naphthaldehyde (0.13 g, 0.0008 mmol) in the presence of 10% NaOH. The reaction was monitored by thin-layer chromatography (TLC) and upon completion, the mixture was neutralized with dilute hydrochloric acid (HCl). Subsequently, a water-chloroform separation was performed to remove excess base. The solvent was then evaporated, and the resulting residue was recrystallized using chloroform to yield the target compound, **MNA**, as a solid. Then evaporate the solvent and the residue was recrystallized by chloroform to give the target compound, **MNA**, as a solid. Yield : 71%. 1H NMR (300 MHz, $CDCl_3$): 8.22-8.17 (d, 1H), 7.57-7.47 (q, 4H), 7.45-7.43 (d, 1H), 7.41-7.29 (m, 6H), 7.14 (s, 1H) 7.09-7.07 (m, 4H), 5.28 (s, 2H)

ppm. ^{13}C NMR (75 MHz, CDCl_3): 196.61, 153.45, 142.21, 134.64, 133.61, 131.81, 131.61, 131.44, 131.29, 130.76, 129.14, 128.99, 128.70, 128.41, 128.21, 127.59, 126.84, 126.15, 125.42, 125.36, 124.29, 123.16, 114.46, 69.53 ppm. LC – MS calcd for $\text{C}_{54}\text{H}_{38}\text{O}_4$: $[\text{M}^+]$ 750.89, found $[\text{M}^+ + \text{H}]^+$ 751.46 (Figure. S2, S4, S6) (Scheme.1).



Scheme 1: Schematic representation of **ONA** and **MNA**

3. RESULT AND DISCUSSION

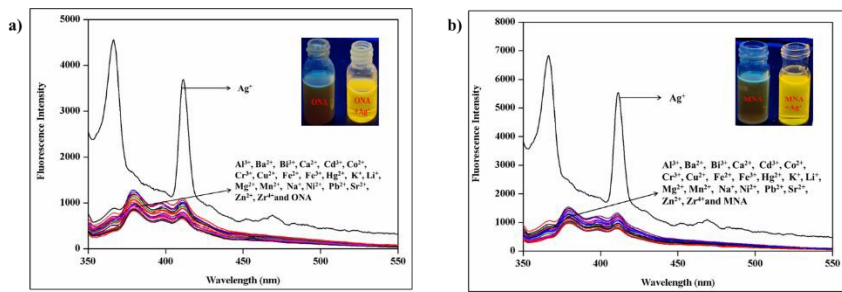
Both probes **ONA** and **MNA** were prepared through a one-step protocol from their respective precursors. The mechanistic pathway involves a series of nucleophilic substitutions, condensations, and recrystallization steps, ultimately leading to the formation of the target compound **ONA**. The reaction begins with the nucleophilic substitution of dibromo ortho-xylene by 2-hydroxy acetonaphthone, facilitated by the base potassium carbonate (K_2CO_3). This step forms a new C-O bond. The resulting compound then reacts with naphthaldehyde in the presence of 10% NaOH, leading to the formation of an intermediate. The intermediate undergoes a condensation reaction, likely an aldol-type condensation resulting in the formation of the **ONA** probe. The final step involves the recrystallization of the crude **ONA** product using chloroform, yielding the pure solid probe. Similar procedure was followed for the synthesis of **MNA**, but instead of dibromo ortho-xylene, dibromo meta-xylene was used. Both the probes were well characterized by the usual spectroscopic and analytical studies.

3.1. Selectivity of **ONA** and **MNA** towards cations

Before conducting fluorescence spectroscopic studies, UV-visible absorption measurements were first performed for both probes, **ONA** and **MNA**, to determine the



appropriate excitation wavelength for subsequent emission experiments (Figure S7). These studies were carried out at three different concentration using methanol as a solvent. Based on the UV-visible spectral analysis, an excitation wavelength of 340 nm was selected for subsequent fluorescence measurements. Furthermore, the absence of any additional or shifted absorption bands in the spectra suggests that no aggregation or supramolecular association of the probe molecules occurred under the employed dilution conditions, indicating that the system remains predominantly in its monomeric form. Probes **ONA** and **MNA**'s selectivity for Ag^+ ion in the presence of several competing metal ions was evaluated under the same experimental environments of $\text{MeOH:H}_2\text{O}(1:1)$ buffer solution at $\text{pH}=7.3$. Only Ag^+ showed a distinct reaction in both probes. Other metal ions Fe^{2+} , Bi^{3+} , Hg^{2+} , Cd^{2+} , Al^{3+} , Na^+ , K^+ , Ca^{2+} , Mg^{2+} , Cu^{2+} , Zn^{2+} , Ni^{2+} , Co^{2+} , Mn^{2+} , Pb^{2+} , Ba^{2+} , Cr^{3+} , Fe^{3+} , Li^+ and Sr^{2+} induced just small emission changes. As seen in figure 1, in the free state, when both probes **ONA** and **MNA** are excited at 340 nm, it exhibited dual emission in weak fluorescence intensity at 380 and 411 nm due to the rotation of carbon oxygen single bond and charge transfer process. When Ag^+ ions were introduced, due to the restriction of C–O bond rotation, inhibition of charge transfer process and the chelation formation, there exhibited a strong fluorescence intensity with hypsochromically shifted in the shorter wavelength from 380 to 366 nm (approximately 14 nm). At the same time, the longer-wavelength band at 411 nm increased notably. These two emission wavelengths are excimer-like emission from π – π interactions between the aromatic moieties (long-wavelength band) and monomeric naphthalene fluorescence (short-wavelength band). Probes **ONA** and **MNA** with Ag^+ ions are also treated with all other metal ions but has not shown any significant spectral changes. It evidences that both probes **ONA** and **MNA** specifically binds with Ag^+ ion with a remarkable blue shift. For the conformation of the selectivity of Ag^+ , interference studies were performed for both probes **ONA** and **MNA**. From figure S8, we can clearly see that both probes bind only with Ag^+ ion and not interfering with any other metal ions mentioned above. Therefore, both probes are selective and sensitive turn-on fluorescent sensors for Ag^+ ions and its widely used for real world sample applications.



View Article Online

DOI: 10.1039/D5SD00202H

Figure 1: Fluorescence emission spectra of a) **ONA**, b) **MNA** against Ag^+ with various metal ions (100 equiv.) were experimented in $\text{MeOH:H}_2\text{O}$ (1:1) HEPES buffer at $\text{pH}= 7.3$ ($\lambda_{\text{ex}} = 340$ nm)

3.2. Binding stoichiometry

To investigate the interaction mechanism and binding affinity of the probes **ONA** and **MNA** toward Ag^+ ions, fluorescence titration experiments were carried out by incremental addition of Ag^+ . In the absence of Ag^+ (0 equiv.), both probes exhibited weak intrinsic fluorescence. Upon gradual addition of Ag^+ , the fluorescence intensity increased steadily up to approximately 30 equivalents, accompanied by a progressive hypsochromic (blue) shift in the emission maximum, indicating the onset of probe–metal coordination. Continued addition of Ag^+ from 30 to 85 equivalents resulted in further enhancement of fluorescence intensity and stabilization of the blue-shifted emission, consistent with the formation of a well-defined probe– Ag^+ complex. Beyond 85 equivalents, no additional changes in either intensity or emission position were observed, demonstrating that the binding sites had reached full saturation. Thus, as shown in Figure 2, both the probes **ONA** and **MNA** achieve a saturated complexation state at around 85 equivalents of Ag^+ , beyond which no further fluorometric response is induced.

The binding stoichiometry was determined using Job's plot analysis, in which the mole fractions of the probes **ONA**, **MNA** and Ag^+ ions were varied but the total concentration remained steady. For both **ONA** and **MNA**, the fluorescence intensity was at its highest at a mole fraction of 0.7, suggesting a ligand-to-metal binding ratio of 1:2 (Figure. S9). This encourages the creation of probes- Ag^+ complex in accordance with the suggested coordination model for both probes. Using the Benesi hiderband (Equation 1), the



association constant (K_a) was calculated to be $0.25 \times 10^4 \text{ M}^{-1}$ for **ONA** and $0.71 \times 10^4 \text{ M}^{-1}$ for **MNA** (Figure 2). For **ONA**, the detection (LOD) and quantification (LOQ) limits were $3.32 \times 10^{-5} \text{ M}$ and $9.97 \times 10^{-4} \text{ M}$ respectively, and $2.57 \times 10^{-6} \text{ M}$ and $7.71 \times 10^{-5} \text{ M}$ for **MNA** respectively. (Figure. S10).

$$I = I_0 + (I_{\max} - I_0) \times K[A] / (1 + K[A]) \quad \text{---(1)}$$

Where, I is the fluorescence intensity, I_0 is the initial fluorescence intensity, I_{\max} is the maximum fluorescence intensity, K is the binding constant and $[A]$ is the metal ion concentration.

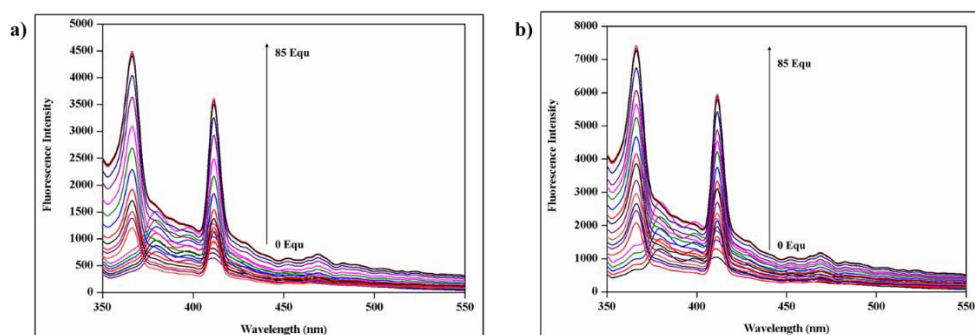


Figure 2: Fluorescence spectral changes of a) **ONA** and b) **MNA** with various concentration of Ag^+ ions (0 to 85 equivalents) ($\lambda_{\text{ex}} = 340 \text{ nm}$)

3.3. Reversibility Studies, Response Time Analysis, and pH Effect

Reversibility studies play a critical role in evaluating the practical utility of chemosensors, particularly for reusable or real-time sensing platforms. A reversible response implies that the sensor-analyte interaction is not permanently destructive and that the system can be regenerated for multiple detection cycles, which is essential for cost-effective environmental monitoring devices, on-site test strips, wearable diagnostic platforms, and microfluidic sensing chips. Demonstrating reversibility also provides mechanistic insight into whether binding is dynamic and equilibrium-controlled rather than irreversible precipitation or chemical transformation. Consequently, reversibility not only enhances the sustainability and economic feasibility of a sensing system but also validates its suitability for dynamic monitoring applications where analyte levels fluctuate over time. Therefore, to test the reversibility of Ag^+ ion detection, studies were conducted by the stepwise addition of Ag^+ and EDTA to the probe solution of **ONA**



and **MNA**. The free probes in the beginning showed a weak fluorescence emission due to the charge transfer (ICT) process. With the addition of Ag^+ (1 equivalent), there was an striking fluorescence enhancement due to the chelation-enhanced fluorescence (CHEF) effect as a result of coordination between Ag^+ and ester oxygen atoms, which restrict the ICT process. With further addition of EDTA, there was a sharp reduction in fluorescence intensity, which can be traced to sequestration of Ag^+ ions by EDTA. This release of Ag^+ destroyed the coordination complex, thus reverting the free probe back to its pre-modified non-emissive state. When further Ag^+ ions added, the intensity of fluorescence once more became quite high, proving the regeneration of the probe– Ag^+ complex. The "on" (Ag^+ addition) and "off" (EDTA addition) cycle of fluorescence response was reproducible for multiple cycles (up to 10 cycles tested), as proved in Figure. S12. This frequent switching behaviour evidently exhibits the reversibility and stability of the sensing process. Such reversibility is very much required after in chemical sensors because this enables the probe to be utilized in several detection cycles without any loss of performance. Further, the full restoration of fluorescence intensity following each addition shows that the binding of Ag^+ with the probe is an immaculate and dynamic equilibration process, not an irreversible chemical conversion.

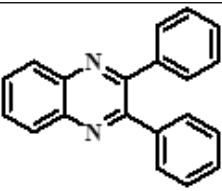
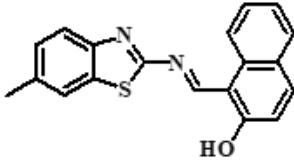
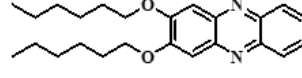
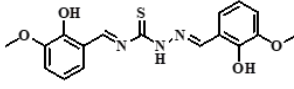
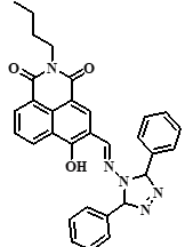
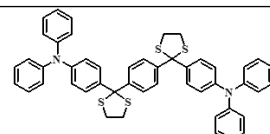
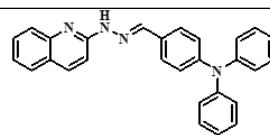
The time-dependent fluorescence response of both probes, **ONA** and **MNA**, in the presence of Ag^+ was examined to assess the kinetics of complex formation. As shown in Figure S11, the fluorescence intensity increased progressively from 0 to approximately 2 minutes, reflecting the gradual formation of the probe– Ag^+ complex. Beyond this point, no further change in emission intensity was observed up to 10 minutes, indicating that the binding equilibrium had been reached. The attainment of a constant fluorescence signal within \sim 2–3 minutes confirms that the complexation process is rapid and kinetically favorable. This short response time is advantageous for real-time or near real-time monitoring and therefore supports the applicability of **ONA** and **MNA** for practical sensing applications where fast detection is essential.

To study the effect of pH on the sensing performance, the fluorescence intensity of the probes were examined under the pH condition ranging from 1.0 to 14.0 without and with Ag^+ ions. The probes itself showed extremely weak emission intensities in

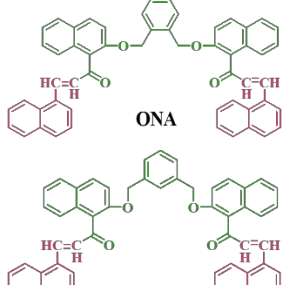
both acidic and basic environments, which are attributable to protonation and deprotonation effects, respectively. At acidic pH (1.0 to 5.0), protonation of the donor oxygen atoms prevents their lone pair accessibility, thus inhibiting Ag^+ coordination and facilitating non-radiative decay channels to quench fluorescence. At basic pH condition (9.0 to 14.0), deprotonation of the functional groups can cause structural distortions or hydrolysis of the probe, while Ag^+ ions can precipitate out as $\text{Ag}_2\text{O}/\text{AgOH}$, both of which inhibit Ag^+ -probes complexation and decrease emission intensity. Conversely, at near neutral pH, the probe is structurally complete, and the donor oxygens are still available for effective coordination of Ag^+ (Figure. S13). This binding process enhances the rigidity of the probes structure and inhibits charge transfer, thus reasoning for a significant fluorescence enhancement. Consequently, the best sensing efficiency of the probe for Ag^+ ions is achieved at near neutral pH, while strongly acidic as well as highly basic conditions are undesirable for the fluorescence response. Therefore, a near neutral pH of 7.3 is the desirable conditions for the practical applications. The quantum yields were calculated for both probes. The emission intensities of both the probes **ONA** and **MNA** were approximately 380 nm. Interestingly, after binding with Ag^+ , the emission intensities of the probes shifted to approximately 366 nm. Hence, an anthracene scaffold was chosen as a reference solution³⁷. The quantum yield of probe **ONA** having 0.074 as the quantum yield, increased to 0.218 upon the addition of Ag^+ ion. Similary, for the probe **MNA** having 0.069 increased to 0.337 after binding with Ag^+ ions. The observed increase in quantum yield suggests that the molecular framework of the probes becomes more rigid upon coordination with Ag^+ ions. Such rigidity typically suppresses non-radiative decay pathways associated with intramolecular rotations or vibrational relaxation, thereby enhancing radiative emission efficiency. This rigidification-induced fluorescence amplification is consistent with the formation of a stable probe- Ag^+ complex that restricts internal degrees of freedom and promotes photon emission.

Table 1: Comparison table of Ag^+ by recently reported compound

Structure	Method	LOD	Mechanism	Application	R

	Fluorometric/Colorimetric	$1.25 \times 10^{-6} \text{ M}$ $7.96 \times 10^{-6} \text{ M}$	PET	Biological sample, cell imaging, real sample analysis	38 View Article Online DOI: 10.1039/D5SD00202H
	Fluorometric/Colorimetric	$0.00389 \mu \text{M}$	PET	Real sample analysis	39
	Fluorometric	-	-	-	40
	Fluorometric	$6.61 \times 10^{-9} \text{ M}$	PET	Test strip, real sample analysis, bio imaging	41
	Fluorometric	18.2 nM	-	Fluorescence imaging in mice cell	42
	Fluorometric	$8.60 \times 10^{-7} \text{ M}$	AIE	Test strip	43
	Fluorometric	17.6 nM	CHEF	Test strip, water sample analysis	44

View Article Online
DOI: 10.1039/D5SD00202H

 <p>ONA</p> <p>MNA</p>	Fluorometric	$3.32 \times 10^{-5} \text{ M}$ $2.57 \times 10^{-6} \text{ M}$	ICT	Real sample analysis, Soil analysis, Anti-counterfeiting, Bio-imaging	Current work
---	--------------	--	-----	---	--------------

4. Spectroscopic and theoretical validations for Probes (ONA and MNA) –Ag⁺ Binding

4.1. Fluorescence lifetime measurement

To gain deeper insight into the excited-state dynamics associated with complexation, time-resolved fluorescence lifetime measurements were carried out for both **ONA** and **MNA** in the absence and presence of Ag⁺ using a MeOH/H₂O (1:1, v/v) system buffered with HEPES at pH 7.3. As shown in Figure S14, the free probe **ONA** exhibited an average lifetime of 0.355 ns, which decreased to 0.149 ns upon addition of Ag⁺. Similarly, the lifetime of **MNA** decreased from 0.363 ns to 0.139 ns after Ag⁺ binding. The pronounced shortening of lifetimes despite an overall enhancement in steady-state fluorescence intensity is characteristic of a static quenching or pre-association mechanism, in which complex formation alters the excited-state relaxation pathways. The results support the interpretation that Ag⁺ coordination inhibits the charge-transfer-mediated non-radiative decay channel that is operative in the free probes, while simultaneously rigidifying the structure and increasing the radiative efficiency observed in steady-state measurements.

4.2. Theoretical calculations

To understand the binding interactions between silver ions (Ag⁺) and the receptor molecules **ONA** and **MNA**, density functional theory (DFT) calculations were performed using the Gaussian 09w software package⁴⁵. The geometries of the free ligands (L1 and L2) and their respective Ag⁺ complexes were optimized using the

B3LYP/LANL2DZ method which is convenient for systems involving transition metals⁴⁶. The optimized molecular geometries of the free ligands and their corresponding Ag^+ complexes are presented in figure. S17. From the figure, the two Ag^+ atom interacts and coordinates with the four oxygen atoms connecting the naphthalene and benzene ring of the probe on either side respectively. The coordination distance between the Ag and O atom were found to be 2.079 Å, 1.920 Å, 1.889 Å and 2.263 Å between the respective for L1 and 2.352 Å, 2.655 Å, 2.558 Å and 2.320 Å for L2. This interaction resulted in alteration of bond lengths and angles at the interaction site and the following are listed in table1. Figure. S18 illustrates the highest occupied molecular orbitals (HOMO) and lowest unoccupied molecular orbitals (LUMO) of the isolate and its complexation with Ag^+ . For the probe **ONA** the HOMO and LUMO orbitals are localized on to the benzene of the probe which delocalizes partly to the naphthalene ring and oxygen atom on the right side at the LUMO level. Subsequently the HOMO-LUMO energy levels (E_{HOMO} and E_{LUMO}) for the free receptor were found to be at -4.55 eV and -1.99eV resulting in and energy gap of 2.56 eV. Upon complexation with $\text{ONA}+\text{Ag}^+$, the complex was found with a localization of HOMO at benzene ring and Ag^+ on the left and delocalization towards the benzene and naphthalene rings entirely on the right side respectively. However, the interaction resulted in stabilization of both E_{HOMO} and stabilization E_{LUMO} energy levels to -10.00 eV and -8.21 eV reducing its energy gap to 1.79 eV. whereas for the metal interaction on **MNA** probe the HOMO and LUMO orbitals are localized on to the benzene of the probe which delocalizes partly to the naphthalene ring and oxygen atom on the right side at the LUMO level. Subsequently the HOMO-LUMO energy levels for the free receptor were found to be at - 5.81 eV and -1.86 eV resulting in and energy gap of 3.85 eV. Upon complexation with L2Ag^+ , the complex was found with a localization of HOMO at benzene ring and delocalization towards the naphthalene rings entirely on the left side respectively. However, the interaction resulted in stabilization of both E_{HOMO} and stabilization E_{LUMO} energy levels to - 9.62 eV and - 7.90 eV respectively resulting in a reduced E_g of 1.72 eV. These findings clearly demonstrate that the binding of Ag^+ to the ligands **ONA** and **MNA** leads to pronounced changes in their electronic properties. The substantial reduction in HOMO–LUMO gaps upon complexation

View Article Online
DOI: 10.3390/Sensors202600202H

highlights the potential of these ligands as effective chemosensor for silver ions, owing to their altered electronic structures and enhanced charge-transfer characteristics.

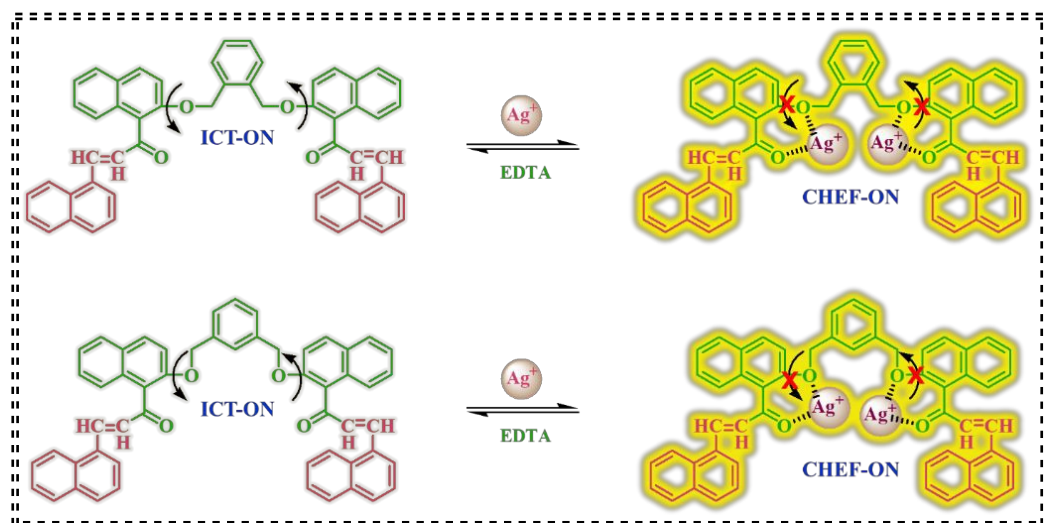
4.3. ^{13}C NMR titration

To further establish the interaction between the probe and Ag^+ , ^{13}C NMR spectra of both probes **ONA** and **MNA** and their Ag^+ complexation (1:2 stoichiometry) were obtained. For that, the 13-carbon nuclear magnetic resonance (^{13}C NMR) spectroscopy analysis of the probes **ONA** and **MNA** were recorded which revealed distinct signals for key functional groups. The carbonyl carbon (C=O) exhibited a characteristic signal at approximately 196 ppm, while the ether carbon (C-O) and methylene group (-CH₂-) resonated at around 153 ppm and 69 ppm, respectively, as indicated in figures S15 and S16. Upon addition of Ag^+ ions to both probes, notable downfield shifts were observed in the ^{13}C NMR spectra. The carbonyl carbon signal shifted to approximately 198 ppm, suggesting strong coordination between the Ag^+ ion and the carbonyl oxygen atom. This deshielding effect can be attributed to the electron-withdrawing nature of the Ag^+ ion, which reduces the electron density around the carbonyl carbon nucleus. Similarly, the C-O peak shifted downfield to around 155 ppm, further supporting the notion of Ag^+ coordination with the oxygen atom. This electron withdrawal effect likely contributes to the observed deshielding of the C-O carbon nucleus. The methylene (-CH₂-) group also exhibited a slight downfield shift to approximately 70 ppm upon Ag^+ complexation. This subtle change suggests a localized alteration in the electronic environment surrounding the methylene group, potentially due to conformational changes or indirect effects of Ag^+ coordination. These chemical shift values are well correlated with fluorescence enhancement, wherein Ag^+ coordination inhibits intramolecular charge transfer (ICT) and triggers the CHEF effect.

4.4. Possible binding mechanism

The interaction between the **ONA** and **MNA** probes and Ag^+ ions is primarily governed by chelation, where the oxygen-rich functional moieties of carbonyl (C=O) and ether (C-O) groups coordinate with the Ag^+ center. Both probes possess these functionalities, rendering them potent ligands for Ag^+ ion coordination, as illustrated in Scheme 2. Upon binding of two Ag^+ ions, intense coordination occurs between the soft

Lewis acidic Ag^+ center and the lone pair of electrons on the carbonyl and ether oxygen atoms. The binding mechanism can be attributed to the following key factors: i) the carbonyl and ether oxygen atoms act as electron donors, forming strong coordinate bonds with the Ag^+ ion through a chelation process, ii) the coordination of Ag^+ ions with the oxygen atoms reduces the electron density at the donor sites, thereby inhibiting the ICT process and iii) the binding of Ag^+ ions restricts the C-O rotation, leading to a conformational change that enhances fluorescence emission. These processes together ultimately trigger a strong fluorescence "turn-on" response. The 1:2 binding stoichiometry between the probes and Ag^+ ions was confirmed through Job's plot analysis, ^{13}C NMR spectroscopy, and fluorescence lifetime decay measurements. The combined results provide valuable insights into the molecular recognition mechanism of the **ONA** and **MNA** probes with Ag^+ ions, highlighting their potential applications in sensing and detection.



Scheme 2: Possible binding mechanism of the probes **ONA** and **MNA** upon addition of Ag^+ ions

5. APPLICATIONS

5.1. Real-World Applicability of ONA and MNA Probes for Ag^+ Ion Detection

The effectiveness of the **ONA** and **MNA** probes in detecting Ag^+ ions in real-world samples was evaluated using the spike and recovery method. Various real-world samples, including pharmaceutical ointments and food samples (barley, sorghum, oats,

black rice, radish, turnip, tapioca, sweet potato, and mushroom), were procured from local markets in Coimbatore, Tamil Nadu, India. The samples were extracted and spiked with three different concentrations of Ag^+ ions (2, 4, and 6 μM). Both probes were then employed to detect the spiked Ag^+ ions, and the recovery percentages were calculated. The results, presented in Tables 2 and 3, demonstrate excellent recovery rates ranging from 89% to 99%. The accuracy of the probes was validated using two independent techniques: fluorescence spectroscopy and inductively coupled plasma mass spectrometry (ICP-MS). The consistency between the two techniques confirms the reliability of the probes in detecting Ag^+ ions in complex real-world samples. The successful application of the **ONA** and **MNA** probes in diverse real-world samples highlights their potential for practical use in environmental monitoring, food safety, and pharmaceutical analysis.

Table 2: Real sample analysis of **ONA** with spiked Ag^+ ions

		Quantified by PL			Quantified by ICP-MS		
Samples	Ag^+ spiked (μM)	Found (μM)	Recovery (%)	RSD	Found (μM)	Recovery (%)	Relative error (%)
Ointment	2	1.93 \pm 0.07	96.5	2.48	1.99 \pm 0.01	99.78	0.22
	4	3.92 \pm 0.08	98.1	1.99	3.97 \pm 0.03	99.32	0.68
	6	6.07 \pm 0.03	101.3	1.87	6.00 \pm 0	100.07	0.07
Barely	2	1.95 \pm 0.05	97.7	0.96	1.97 \pm 0.03	99.65	1.35
	4	3.95 \pm 0.05	98.7	2.38	3.93 \pm 0.07	99.27	1.73
	6	5.97 \pm 0.03	99.6	2.36	5.94 \pm 0.06	99.12	0.88
Sorghum	2	1.90 \pm 0.10	95.2	1.14	1.99 \pm 0.01	99.52	0.48
	4	3.85 \pm 0.15	96.3	1.64	4.01 \pm 0.01	99.84	0.16
	6	5.84 \pm 0.16	97.4	1.62	6.09 \pm 0.09	99.64	0.36
Oats	2	1.88 \pm 0.12	94.3	1.89	1.97 \pm 0.03	98.76	1.24
	4	3.82 \pm 0.18	95.7	1.14	3.94 \pm 0.06	98.76	1.33
	6	5.87 \pm 0.13	97.9	0.63	5.99 \pm 0.01	99.89	0.11
Black rice	2	1.93 \pm 0.07	96.7	1.64	2.00 \pm 0	100.41	0.41

	4	3.90±0.10	97.5	3.75	3.98±0.02	99.71	0.29
	6	5.98±0.02	99.8	3.71	6.06±0.06	100.05	0.05
Radish	2	1.85±0.15	92.7	2.09	1.94±0.06	97.39	2.61
	4	3.83±0.17	95.8	4.26	3.94±0.06	98.56	1.44
	6	5.78±0.22	96.4	3.91	5.97±0.03	99.65	0.35
Turnip	2	1.78±0.22	89.2	3.41	2.00±0	100.23	0.23
	4	3.75±0.25	93.7	2.56	3.99±0.01	99.97	0.03
	6	5.72±0.28	95.3	2.47	6.10±0.10	100.83	0.83
Tapioca	2	1.81±0.19	90.7	3.06	1.99±0.01	99.67	0.33
	4	3.73±0.27	93.2	3.27	3.95±0.05	98.87	1.13
	6	5.78±0.22	96.4	3.31	5.99±0.01	99.93	0.07
Sweet potato	2	1.81±0.19	90.3	3.84	1.98±0.02	99.23	0.77
	4	3.77±0.23	94.3	4.29	3.98±0.02	99.69	0.31
	6	5.85±0.15	97.5	4.28	5.91±0.09	98.56	1.44
Mushroom	2	1.79±0.21	89.5	3.72	1.99±0.01	99.96	0.04
	4	3.74±0.26	93.6	2.78	3.93±0.07	98.47	1.53
	6	5.78±0.22	96.4	2.81	5.99±0.01	99.94	0.06

Table 3: Real sample analysis of MNA with spiked Ag⁺ ions

		Quantified by PL			Quantified by ICP-MS		
Samples	Ag ⁺ spiked (μM)	Found (μM)	Recovery (%)	RSD	Found (μM)	Recovery (%)	Relative error (%)
Ointment	2	1.97±0.03	98.5	1.94	1.99±0.01	99.78	0.22
	4	3.98±0.02	99.7	4.13	3.97±0.03	99.32	0.68
	6	6.14±0.14	102.3	4.09	6.00±0	100.07	0.07
Barely	2	1.88±0.12	94.3	2.19	1.97±0.03	99.65	1.35

	4	3.91±0.09	97.7	1.95	3.93±0.07	99.27	0.73
	6	5.89±0.11	98.2	1.82	5.94±0.06	99.12	0.88
Sorghum	2	1.89±0.11	94.7	1.46	1.99±0.01	99.52	0.48
	4	3.85±0.15	96.3	2.14	4.01±0.01	99.84	0.16
	6	5.85±0.15	97.5	2.10	6.09±0.09	99.64	0.36
Oats	2	1.87±0.13	93.5	2.31	1.97±0.03	98.76	1.24
	4	3.81±0.19	95.3	4.09	3.94±0.06	98.76	1.33
	6	5.87±0.13	97.9	4.18	5.99±0.01	99.89	0.11
Black rice	2	1.81±0.19	90.3	2.76	2.00±0	100.41	0.41
	4	3.70±0.30	92.5	2.26	3.98±0.02	99.71	0.29
	6	5.72±0.28	95.4	2.32	6.06±0.06	100.05	0.05
Radish	2	1.83±0.17	91.3	3.49	1.94±0.06	97.39	2.61
	4	3.78±0.22	94.6	2.36	3.94±0.06	98.56	1.44
	6	5.87±0.13	97.9	2.55	5.97±0.03	99.65	0.35
Turnip	2	1.87±0.13	93.6	2.71	2.00±0	100.23	0.23
	4	3.91±0.09	97.8	3.31	3.99±0.01	99.97	0.03
	6	5.90±0.10	98.4	3.14	6.10±0.10	100.83	0.83
Tapioca	2	1.81±0.19	92.6	2.62	1.99±0.01	99.67	0.33
	4	3.73±0.27	94.3	1.71	3.95±0.05	98.87	1.13
	6	5.78±0.22	97.5	1.14	5.99±0.01	99.93	0.07
Sweet potato	2	1.85±0.15	95.3	1.68	1.98±0.02	99.23	0.77
	4	3.85±0.15	96.4	3.64	3.98±0.02	99.69	0.31
	6	5.91±0.09	98.5	3.76	5.91±0.09	98.56	1.44
Mushroom	2	1.83±0.17	91.7	3.01	1.99±0.01	99.96	0.04
	4	3.73±0.27	93.3	2.15	3.93±0.07	98.47	1.53
	6	5.83±0.17	97.2	1.67	5.99±0.01	99.94	0.06

5.2. Detection of Ag⁺ ions in soil samples using ONA and MNA Probes

To evaluate the detection of Ag⁺ ions in soil, four different types of soils (stream soil, ash soil, red soil and grass soil) were collected from various parts of Namakkal

district, Tamil Nadu, India. Those soils were air-dried and sieved to $>250\mu\text{m}$, then extracted the soil under 30mins of sonication by using the solvent mixture of methanol:water (1:1). In this extract spiked with $20\mu\text{M}$ concentration of Ag^+ ions and were leftover night to absorb the Ag^+ . Then the soil was added with probes solution of **ONA** and **MNA**. As seen in figure. 3, the pale-yellow colour was visible under the naked eye and strong bright yellow fluorescence were observed under UV 365nm. This clearly evidence that, both probes **ONA** and **MNA** were successfully utilized for the detection of Ag^+ ions in environmental samples.

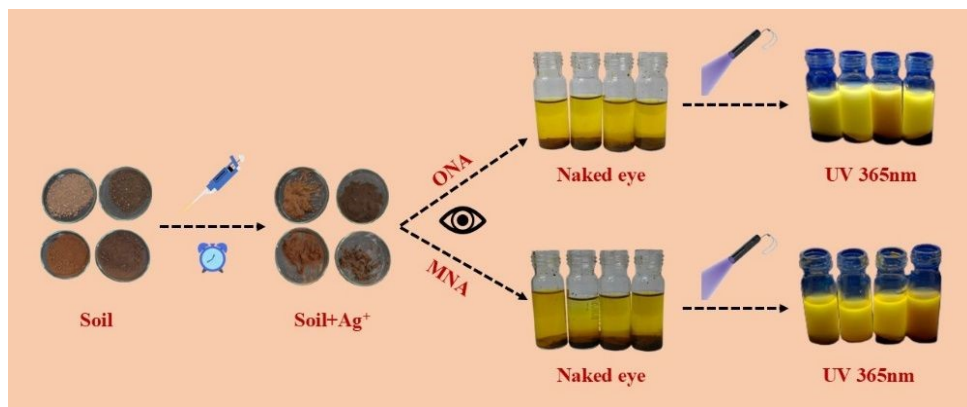


Figure 3: Detection of Ag^+ ions in soil samples by using probes **ONA** and **MNA**

5.3. Anti-counterfeiting application

A stamping method was employed by immersing cotton pads with probes (**ONA** and **MNA**)+ Ag^+ complex solution. This solution was used as an ink for stamping on Whatman filter paper. The stamped region was mildly visible in the naked eye as pale yellow in colour. When the UV light of 365 nm was passed, it showed a bright yellow fluorescence with clear stamping patterns as seen in figure. 4. This non-destructive fluorescence switching behaviour highlights the potential application in security printing and anticounterfeiting technologies⁴⁷.

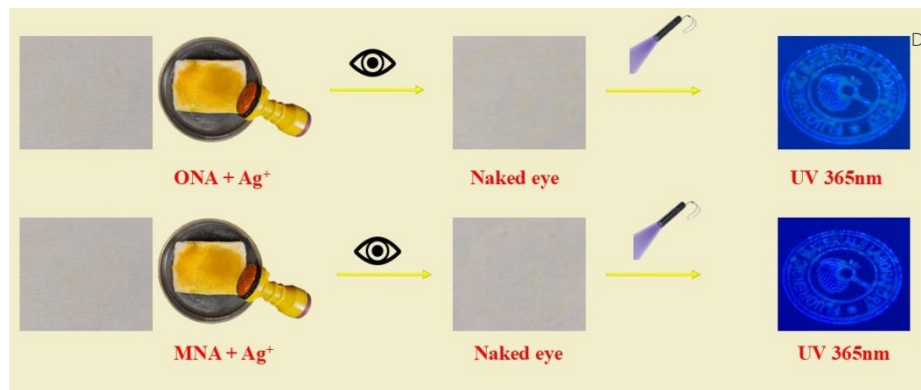


Figure 4: visualization of fluorescence stamping by using complexation solution of **ONA** and **MNA** with Ag^+ ions

5.3. Visualizing Ag^+ Ions in Biological Systems using Fluorescent Probes **ONA** and **MNA**

This study aims to investigate the detection of Ag^+ ions in *Escherichia coli* using fluorescent probes **ONA** and **MNA**, visualized through confocal laser scanning microscopy (CLSM) in a co-cultured medium. The medium was scanned at 40x magnification (bright field) with the excitation. As shown in Figure. 5, probes **ONA** and **MNA** and its complexation with Ag^+ ions were employed by using brightfield, confocal and overlay imaging. Both the probes **ONA** and **MNA** ($10 \mu\text{M}$) showed weak fluorescence activity. The fluorescence activity of the complexation was detected through the green channel upon the addition of $20 \mu\text{M}$ of Ag^+ ions. This finding indicates that after Ag^+ binding, both probes exhibit high fluorescence activity through the green channel. The cell imaging findings support this concept of that confocal scanning microscopy detects higher activity in *E. coli* bacteria using the complexation mechanism, suggesting that both probes can be an effective fluorescent compound for the detection of Ag^+ ions in biological samples⁴⁸. The MTT reduction test was used to assess the cytotoxicity and cell viability of the probes **ONA** and **MNA** and their *invitro* anticancer action was compared with the MCF-7 cell line based on this approach. Table S3 displays the calculated IC50 values from MCF-7 cells, whereas fig. S20 shows the cytotoxicity of the probes **ONA** and **MNA**.



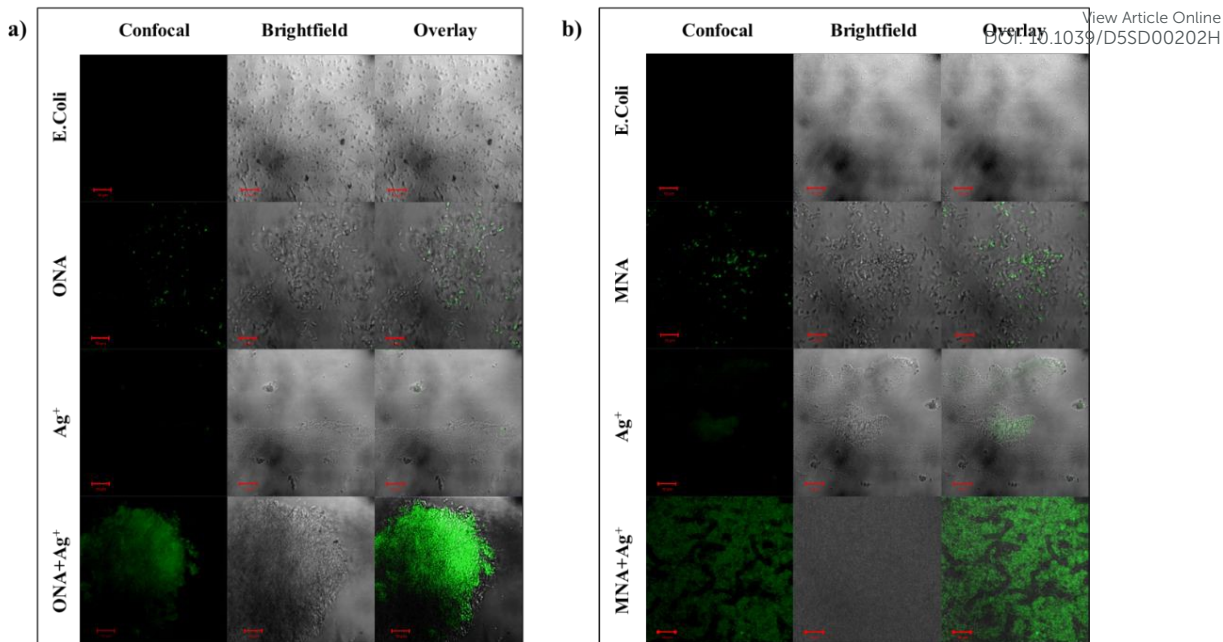


Figure 5: Confocal microscopic imaging was performed on *E.coli* pathogen treated with probes **ONA** and **MNA** in presence and absence of Ag^+ ions in confocal, bright field and overlay. [Scale 10 μM].

6. CONCLUSION

Our experimental results demonstrate that **ONA** and **MNA** probes are highly selective fluorescent sensors for detecting Ag^+ ions in $\text{MeOH:H}_2\text{O}$ (1:1) solution buffered with HEPES (pH 7.3). The sensing mechanism involves restriction of C-O rotation and inhibition of intramolecular charge transfer (ICT), resulting in a hypsochromic shift. The 1:2 binding stoichiometry between probes and Ag^+ ions was confirmed by Job's plot, Benesi-Hildebrand plot, fluorescence lifetime measurements, and ^{13}C NMR spectroscopy. The probes were successfully applied to detect Ag^+ ions in real-world samples, including food (millets, vegetables), pharmaceuticals (ointments), and environmental samples (soil), as well as in live-cell imaging of *E. coli* bacterial cells, demonstrating biocompatibility. Additionally, the probes' complexation solution was used as a fluorescence-based stamp-ink method for anti-counterfeiting, highlighting their potential for security applications. Further works on the derivation of the probes and other potential applications are currently underway in our laboratory.

Acknowledgement



Narmatha Ganesan, Kavanya Srinivasan and Elizabeth Antony are very much thankful to Karunya Institute of Technology and Sciences (deemed to be university) for providing the financial support through Research Associateship fellowship. The authors gratefully thank the Central NMR facility at Karunya Institute of Technology and Sciences.

References

- 1 A. Melaiye and W. J. Youngs, *Expert Opin. Ther. Pat.*, 2005, **15**, 125–130.
- 2 A. Panáček, M. Kolář, R. Večeřová, R. Prucek, J. Soukupová, V. Kryštof, P. Hamal, R. Zbořil and L. Kvítek, *Biomaterials*, 2009, **30**, 6333–6340.
- 3 S. R. Isbel, S. A. Patil and A. Bugarin, *Inorganica Chim. Acta*, 2024, **563**, 121899.
- 4 J. K. Jose, B. Mishra, K. P. Kootery, C. T. Cherian, B. P. Tripathi, S. Sarojini and M. Balachandran, *Mater. Sci. Eng. B*, 2023, **297**, 116789.
- 5 Z. Aziz, S. F. Abu and N. J. Chong, *Burns*, 2012, **38**, 307–318.
- 6 T. Bjarnsholt, K. Kirketerp-Møller, S. Kristiansen, R. Phipps, A. K. Nielsen, P. Ø. Jensen, N. Høiby and M. Givskov, *APMIS*, 2007, **115**, 921–928.
- 7 H. M. Assar, N. H. and Hamouda, 2010.
- 8 I. Zajac, J. Szulc and B. Gutarowska, *J. Cult. Herit.*, 2021, **51**, 59–70.
- 9 T. M. Vu, S. Johnston, D. Simondson, C. K. Nguyen, T. D. Nguyen, D. Van Zeil, R. K. Hocking, D. R. Macfarlane and A. N. Simonov, *ACS Catal.*, 2024, **14**, 10974–10986.
- 10 S. Payamifar, H. Sarreshtehdar Aslaheh and A. Poursattar Marjani, *J. Organomet. Chem.*, 2025, **1038**, 123776.
- 11 H. Li and H. Xu, *Environ. Res.*, 2024, **248**, 118313.
- 12 A. May, Z. Kopecki, B. Carney and A. Cowin, *ANZ J. Surg.*, 2022, **92**, 379–384.

View Article Online
DOI: 10.1039/D5SD00202H

13 H. Liang, M. S. Mirinejad, A. Asefnejad, H. Baharifar, X. Li, S. Saber, Samandari, D. Toghraie and A. Khandan, *Mater. Chem. Phys.*, 2022, **279**, 125770.

14 *Mater. Sci. Eng. C*, 2021, **128**, 112342.

15 M. J. Eckelman and T. E. Graedel, *Environ. Sci. Technol.*, 2007, **41**, 6283–6289.

16 H. Li, D. Qiao, M. Chu, L. Guo, Z. Sun, Y. Fan, S. Q. Ni, C. H. Tung and Y. Wang, *Environ. Sci. Technol.*, 2023, **57**, 20822–20829.

17 S. L. Chiam, A. T. Le, S. Y. Pung and F. Y. Yeoh, *Int. J. Miner. Metall. Mater.*, 2021, **28**, 325–334.

18 M. K. Y. Soliman, S. S. Salem, M. Abu-Elghait and M. S. Azab, *Appl. Biochem. Biotechnol.*, 2023, **195**, 1158–1183.

19 N. Tripathi and M. K. Goshisht, *ACS Appl. Bio Mater.*, 2022, **5**, 1391–1463.

20 H. T. Ratte, *Environ. Toxicol. Chem.*, 1999, **18**, 89–108.

21 M. N. Croteau, S. K. Misra, S. N. Luoma and E. Valsami-Jones, *Environ. Sci. Technol.*, 2011, **45**, 6600–6607.

22 X. Li, C. Batchelor-Mcauley and R. G. Compton, *ACS Sensors*, 2019, **4**, 464–470.

23 J. Kang, M. Choi, J. Y. Kwon, E. Y. Lee and J. Yoon, *J. Org. Chem.*, 2002, **67**, 4384–4386.

24 H. M. Al-Saidi and S. Khan, *Crit. Rev. Anal. Chem.*, 2024, **54**, 1810–1836.

25 A. F. Lagalante, 2007, 37–41.

26 T. Van Acker, S. Theiner, E. Bolea-Fernandez, F. Vanhaecke and G. Koellensperger, *Nat. Rev. Methods Prim.*, 2023, **3**, 4455–4486.

27 Y. Habata, M. Ikeda, S. Yamada, H. Takahashi, S. Ueno, T. Suzuki and S. Kuwahara, *Org. Lett.*, 2012, **14**, 4576–4579.

28 A. D. Arulraj, R. Devasenathipathy, S. M. Chen, V. S. Vasantha and S. F. Wang, *Sens. Bio-Sensing Res.*, 2015, **6**, 19–24. [View Article Online](https://doi.org/10.1039/D5SD00202H)

29 C. Y. Li, F. Xu and Y. F. Li, *Spectrochim. Acta Part A Mol. Biomol. Spectrosc.*, 2010, **76**, 197–201.

30 Y. Qi, H. Xu and H. Chen, *ACS Omega*, 2025, **10**, 11743–11754.

31 P. Gunasekaran, C. Immanuel David, S. Shanmugam, K. Ramanagul, R. Rajendran, V. Gothandapani, V. R. Kannan, J. Prabhu and R. Nandhakumar, *J. Agric. Food Chem.*, 2023, **71**, 802–814.

32 G. Narmatha, E. Antony, G. Prabakaran, K. Sundaram, S. Ravi, S. Abisha Nancy, A. Abiram, K. Parvatham, V. Rajesh Kannan, A. I. Almansour, R. Suresh Kumar and R. Nandhakumar, *J. Photochem. Photobiol. A Chem.*, 2025, 116029.

33 J. Dessimou, A. Mitra, K. Tabbasum, G. S. Baghel and C. P. Rao, *J. Org. Chem.*, 2012, **77**, 371–378.

34 G. Prabakaran, K. Velmurugan, C. I. David, S. P. Makarios, A. Abiram, R. Suresh, A. I. Almansour, K. Perumal and R. Nandhakumar, *J. Mol. Liq.*, 2023, **388**, 122733.

35 S. M. Kumar and S. K. Iyer, *J. Photochem. Photobiol. A Chem.*, 2025, **462**, 116212.

36 N. Ganesan, K. Srinivasan, E. Antony, A. N. Sukumar, A. Angamuthu, J. G. Małecki and R. Nandhakumar, *ChemPhotoChem*, 2025, **00**, 161.

37 K. Lawson-wood, *Fluoresc. Spectrosc.*, 2018, 1–5.

38 S. Dutta, V. Sharma, A. Pandey, D. Kumar, D. Sahu and G. K. Patra, *J. Fluoresc.*, 2025, **025**, 04528.

39 G. M. Abu-Taweel, H. M. Al-Saidi, M. Alshareef, M. A. M. Alhamami, J. S. Algethami and S. S. Alharthi, *J. Fluoresc.*, 2025, **35**, 221–236.

40 H. V. Barkale and N. Dey, *J. Mol. Struct.*, 2024, **1303**, 137427.

41 K. B. Hiremath and M. Shivashankar, *J. Mol. Struct.*, 2024, **1302**, 137490. [View Article Online](#)
DOI:10.1039/D5SD00202H

42 Y. Xu, Y. Zhu, F. Yang, Y. Gao and Y. Gao, *New J. Chem.*, 2024, **49**, 2694–2702.

43 Z. Ruan, X. Dong, T. Long, S. Liu, Y. Chen and J. Lin, *J. Mater. Chem. C*, 2024, **12**, 7572–7579.

44 J. Sengottaiyan, K. Parvathi, S. Murukesan, B. Karpagam, J. Rajesh and G. Rajagopal, *ChemistrySelect*, 2025, **10**, 1–9.

45 *Methods Electron. Struct. Theory*, DOI:10.1007/978-1-4757-0887-5.

46 C. Adamo and D. Jacquemin, *Chem. Soc. Rev.*, 2013, **42**, 845–856.

47 K. Abou-Melha, *Arab. J. Chem.*, 2022, **15**, 103604.

48 M. B. I. Mohamed, T. S. Aysha, T. M. Elmorsi, M. El-Sedik, S. T. Omara, E. Shaban, O. M. Kandil and A. H. Bedair, *J. Fluoresc.*, 2020, **30**, 601–612.

ICT-Driven Ag⁺ Detection Using Xylene-spacer integrated Naphthalene Probes as Fluorescent Chemosensors: Selectivity, Practical Monitoring, and Anticounterfeiting

Narmatha Ganesan^a, Kavanya Srinivasan^a, Elizabeth Antony^a, hab. Jan G. Malecki^b, Abisha Nancy Sukumar^c, Abiram Angamuthu^{d,*}, J. Prabhu^a, Raju Nandhakumara^{a,*}

^aFluorescent Materials Lab, Division of Physical Science, Karunya Institute of Technology and Sciences, (Deemed-to-be University), Karunya Nagar, Coimbatore - 641 114, India.

*E-mail: nandhakumar@karunya.edu

^b WSB University, Cieplaka 1c, Dąbrowa Górnica, Poland

^c Department of physics, Karpagam College of Engineering, Coimbatore, Tamil Nadu, India

^d Department of physics, Rathinam Technical Campus, Coimbatore- 641021, Tamil Nadu, India

*E-mail: aabiram@gmail.com

Data availability statement:

All data supporting the findings of this study are available within the article and its Supplementary Information files.

